Hindawi
Adsorption Science & Technology
Volume 2023, Article ID 5512881, 16 pages
https://doi.org/10.1155/2023/5512881

Research Article

Efficient Removal of Paraquat Pollutants Using Magnetic Biochar Derived from Corn Husk Waste: A Sustainable Approach for Water Remediation

Sakonsupa Damdib,[1] **Adisak Siyasukh**,[2,3] **Bhawaranchat Vanichsetakul**,[1] **Phamornsiri Phamornpiboon**,[2] **Chanchana Thanachayanont**,[4] **Patiparn Punyapalakul**,[5,6] **and Nattaporn Tonanon**[1]

[1]*Bio-Circular-Green Economy Technology and Engineering Center (BCGeTEC), Department of Chemical Engineering, Faculty of Engineering, Chulalongkorn University, Bangkok 10330, Thailand*
[2]*Research Laboratory of Pollution Treatment and Environmental Material (PTEM), Department of Industrial Chemistry, Faculty of Science, Chiang Mai University, Chiang Mai 50200, Thailand*
[3]*Materials Science Research Center, Faculty of Science, Chiang Mai University, Chiang Mai 50200, Thailand*
[4]*National Metal and Materials Technology Center, 114 Thailand Science Park, Paholyothin Rd., Klong 1, Klong Luang 12120, Thailand*
[5]*Department of Environmental Engineering, Faculty of Engineering, Chulalongkorn University, Bangkok 10330, Thailand*
[6]*Research Unit Control of Emerging Micropollutants in Environment, Chulalongkorn University, Bangkok 10330, Thailand*

Correspondence should be addressed to Adisak Siyasukh; adisak.si@cmu.ac.th and Nattaporn Tonanon; nattaporn.t@chula.ac.th

Received 26 February 2023; Revised 23 August 2023; Accepted 2 September 2023; Published 15 September 2023

Academic Editor: Nguyen Hai Tran

Due to the widespread production of maize, the waste created by this crop has become a serious concern. This study applied the concept of waste circulation to the production of magnetic biochar from corn husk waste to remediate paraquat-contaminated water. Magnetic biochar (MB) was produced by impregnating maize husks with iron and carbonizing the residue in a nitrogen environment. Carbonized MB at the temperature of 850°C (MB-01-850) exhibited a combination of microporous and mesoporous structures ($V_{meso} = 0.30\ cm^3/g$, $V_{micro} = 0.12\ cm^3/g$), while biochar created only a microporous structure ($V_{micro} = 0.11\ cm^3/g$). According to the findings, $Fe(NO_3)_3$ significantly affected the increase in mesopore formation after carbonization. In addition, biochar exhibits excellent magnetic responsiveness. MB-01-850 reached equilibrium within approximately 20 min in synthetic water. Batch adsorption studies showed that MB-01-850 had maximum adsorption capacities (Q_0) of 34.97 mg/g and 31.63 mg/g for synthetic and natural water, respectively. The unmodified biochar (without mesopores) had a Q_0 of 4.08 mg/g. This indicates that the presence of mesopores improves the effectiveness of paraquat adsorption. Additionally, the adsorption performance of magnetic biochar exhibited no statistically significant variance when tested under natural water conditions. Furthermore, magnetic biochar demonstrates impressive regeneration capacity, allowing it to be regenerated almost entirely for a minimum of four cycles using a sodium hydroxide (NaOH) solution with a concentration equal to or greater than 0.5 M.

1. Introduction

The increase in agricultural waste has been a serious concern over the last few decades, with maize being one of the most produced crops in the world. Significant by-products of maize production, including cobs, stems, leaves, and husks, are produced during harvest. Unfortunately, the combustion of these agricultural wastes releases several air pollutants, such as solid greenhouse gases, and suspended particulate matter, such as PM2.5 and PM10. These poisons have been

shown to be harmful to human health and the environment [1]. Therefore, the development and implementation of sustainable disposal options for agricultural waste are essential to reduce this problem. The cellulose, hemicellulose, and lignin of maize husk may be utilized to produce biochar, a porous carbon substance. Biochar is widely utilized in environmental applications due to its distinct characteristics, ecological compatibility, cost-effectiveness, and robustness in both mechanical and thermal aspects [2, 3]. In particular, it effectively removes pollutants from wastewater by acting as an adsorbent. It is important to note that biochar serves as an adsorbent for removing pollutants from wastewater. However, unmodified biochar has limitations in water treatment applications because of its low adsorption capacity, inadequate selectivity, limited reusability, and challenges in regeneration [4]. Consequently, modification of biochar is imperative to enhance its adsorption capacity and practical efficacy. Several methods have been used to modify the properties of biochar, with physical and chemical modifications being the most common ones.

Physical modification involves subjecting biochar to high-temperature steam and gas, which effectively increases its surface area by modifying its pore structure, whereas chemical modification [5] represents the predominant technique. These include acid modification [6, 7], alkalinity modification [8], modification using metal salts or oxidizing agents [9], and modification with carbonaceous materials such as graphene and carbon nanotubes [10].

Moreover, unmodified biochar with a fine particle size poses challenges in terms of separation from aqueous solutions after the adsorption process. This difficulty hampers its reusability and transforms it into a secondary pollutant. Therefore, modifying the magnetic properties of biochar is highly desirable because it enables efficient separation from aqueous solutions in the presence of an external magnetic field. This characteristic significantly facilitates the separation and regeneration processes. Magnetic biochar can be produced through various techniques, including impregnation-pyrolysis, coprecipitation, reductive codeposition, and hydrothermal carbonization [11, 12]. Typically, magnetic biochar is synthesized using impregnation-pyrolysis processes with activators, such as iron chloride ($FeCl_3$) [13] or iron sulfate heptahydrate ($FeSO_4{\cdot}7H_2O$) [14]. Several studies have shown that impregnating $Fe(NO_3)_3$ onto biomass not only enhances its magnetic properties but also induces a mesoporous structure in the adsorbent material [15, 16], making it particularly suitable for water treatment applications.

Intensive seasonal farming, especially maize cultivation, generates a substantial amount of wastewater that becomes contaminated with pesticides or herbicides. Unfortunately, these contaminants can potentially infiltrate groundwater and surface water sources, thereby posing a significant environmental risk. In line with the principles of waste cycling and pollutant elimination, the use of biochar derived from corn waste has emerged as an ideal solution to address the problem of pesticide or herbicide removal from contaminated wastewater. This sustainable approach not only effectively addresses the issue of pollutant removal but also maximizes the utilization of agricultural waste materials. When corn waste is utilized in biochar as an adsorbent, harmful pesticides or herbicides can be efficiently captured and removed from wastewater, thereby reducing the risk of further water pollution. This approach not only offers a solution to the environmental challenges posed by intensive farming practices but also promotes the circular economy by transforming agricultural waste into a valuable resource for water treatment.

Paraquat is a highly toxic herbicide used worldwide to control weeds in agricultural and nonagricultural settings. Paraquat (PQ; 1,1-dimethyl-4,4-bipyridyl dichloride) or methyl viologen is a nonselective contact herbicide used to control broadleaf weeds and grasses by inhibiting photosynthesis and destroying plant organelles [17]. It is now known to be harmful to both humans and animals. Furthermore, it may be an environmental factor in neurodegenerative diseases such as Parkinson's disease [18, 19]. In particular, PQ exhibits considerable water solubility (620 g/L at 25°C) in the environment [20], thereby raising the potential risk of contamination from water sources. Consequently, these contaminants significantly affect aquatic ecosystems and human health. Additionally, it forms strong bonds with the soil particles, resulting in long-lasting bonds. [21]. In Thailand, PQ concentrations are 1.5 to 18.9 μg/L for groundwater and 9.3 to 87.0 μg/L for surface water [22]. European standards require that the concentration of PQ in water sources be no more than 0.1 μg/L for drinking water and 1-3 μg/L for surface water [23]. These values suggest that PQ residues in water threaten human health and the environment, especially during the rainy season. Given the health and environmental risks associated with PQ use, many countries have restricted or banned its use. However, paraquat is still widely used in some parts of the world due to its effectiveness and low cost [24]. Thus, removal of PQ from contaminated water sources is a challenging and attractive task.

Several techniques, such as ozonation [25], photocatalytic processes, Fenton reactions [25, 26], and adsorption, have been applied to remove contaminated PQ from water sources. Among the many techniques, adsorption is one of the best methods for treating wastewater, with high efficiency, low cost, ease of operation, and absence of hazardous by-product formation [27, 28]. Various adsorbents have been used for wastewater treatment, including natural adsorbents [29, 30], activated carbon [31], carbon-based materials (carbon nanotubes), and biochar. The prevalence of biochar derived from agricultural residues has significantly increased in recent years. This increased recognition is primarily attributed to its effectiveness in addressing environmental problems and suitability as an adsorbent to remove pollution.

This study is aimed at developing an affordable adsorbent material derived from agricultural waste to treat water sources contaminated with PQ. To achieve this objective, we used corn husks as the carbon precursor and synthesized magnetic biochar materials by impregnating corn husks with $Fe(NO_3)_3$ followed by carbonization under a nitrogen atmosphere. The resulting biochars were used as adsorbents to remove PQ from aqueous solutions. Our research focused

on investigating the influence of $Fe(NO_3)_3$ on the properties of the adsorbent and understanding the underlying mechanism of paraquat (PQ) adsorption using magnetic biochar under both synthetic water (DI water) and natural water conditions. In addition, a study on the regeneration of magnetic biochar was conducted.

2. Materials and Methods

2.1. Materials and Chemicals. Corn husks were collected from an agricultural area in Lamphun Province. After cutting into small pieces, they were washed with DI water and dried at 80°C for 24 h. Analytical standard paraquat ($C_{12}H_{14}Cl_2N_2$, PESTANAL) was purchased from Sigma-Aldrich. Gramoxone ($C_{12}H_{14}Cl_2N_2$, 37% paraquat) and iron(III) nitrate nonahydrate ($Fe(NO_3)_3{\cdot}9H_2O$, >99%) were purchased from Syngenta Thailand and AnalaR BDH, respectively.

2.2. Preparation of Magnetic Biochars and Biochar. To prepare the magnetic biochars, the corn husks were immersed in $Fe(NO_3)_3$ solution at 80°C for 2 h, dried at 80°C for 24 h, and carbonized in a nitrogen atmosphere at a heating rate of 10°C/min for 2 h. The preparation conditions of the samples are listed in Table 1.

2.3. Paraquat Adsorption Experiments. The experiments were performed using a batch process. It was carried out by contacting adsorbent dosages (0.25-3.00 g/L) with 100 mL of PQ solution with varied initial concentrations (5-200 mg/L) and shaken at 200 rpm at 30 to 50°C until the equilibrium time was reached. The pH range of 4 to 10 was examined at an initial PQ concentration of 40 mg/L, and the pH levels were controlled using buffer solutions containing acetic acid/sodium acetate and ammonium hydroxide/ammonium chloride. PQ concentration was analyzed using an ultraviolet-visible spectrophotometer (SPECORD® 50 PLUS, Analytik Jena) at a maximum absorbance wavelength of 258 nm. The amount of PQ at equilibrium (q_e) and the removal percentage (%Removal) were calculated using

$$q_e = \frac{(C_0 - C_e)V}{W}, \tag{1}$$

$$\%\text{Removal} = \frac{(C_0 - C_e)}{C_0} \times 100, \tag{2}$$

where C_0 and C_e are the initial and equilibrium concentrations of PQ (mg/L), respectively, V is the volume of the solution (L), and W is the weight of the adsorbent (g).

The reusability of spent magnetic biochar was investigated by comparing the adsorbent with and without regeneration. The experiments were carried out at an initial concentration, adsorbent dosage, temperature, pH, and contact time of 20 mg/L, 2.0 g/L, 30°C, 7, and 24 h, respectively. The regenerated sorbent was immersed in NaOH solutions with concentrations of 0.1, 0.5, and 1.0 M for 24 h [32]. The mixture was dried and subjected to subsequent adsorption under the same conditions. This cycle was repeated multiple times, until four trial cycles were completed.

Table 1: Synthesis conditions of magnetic biochars and biochar derived from corn husk.

Samples	Concentration of $Fe(NO_3)_3$ (M)	Carbonization temperature (°C)
B-00-850	0.00	850
MB-001-850	0.01	850
MB-005-850	0.05	850
MB-01-850	0.10	850
MB-01-750	0.10	750
MB-01-650	0.10	650
MB-01-550	0.10	550

2.3.1. Adsorption Isotherm Models. The Langmuir and Freundlich models were used to describe the adsorption mechanism of PQ.

The Langmuir isotherm model [33, 34] is expressed by

$$q_e = \frac{Q_0 b C_e}{1 + bC_e}, \tag{3}$$

where q_e is the amount of PQ at equilibrium (mg/g), Q_0 is the maximum adsorption capacity (mg/g), and b is the Langmuir constant (L/mg).

The Freundlich isotherm model [34, 35] is determined by

$$q_e = K_F C_e^{1/n}, \tag{4}$$

where K_F is the Freundlich constant ((mg/g)(L/mg)$^{1/n}$) and n is the intensity of adsorption.

2.3.2. Thermodynamic Adsorption Models. The thermodynamic parameters, including the change of standard enthalpy (ΔH^0), change of standard entropy (ΔS^0), and change of standard Gibbs free energy (ΔG^0), were calculated using the linearized van't Hoff equation as given in

$$\ln K_{EQ}^0 = -\left(\frac{\Delta H^0}{R}\right)\frac{1}{T} + \frac{\Delta S^0}{R}, \tag{5}$$

where K_{EQ}^0, R, and T are the equilibrium constant, universal gas constant (8.314 J/mol·K), and temperature (K), respectively.

The K_{EQ}^0 is calculated from [36]

$$K_{EQ}^0 = b \times MW_a \times 1000 \times \frac{C_a^0}{\gamma_a}, \tag{6}$$

where b (L/mg) is the Langmuir constant, MW_a (g/mol) is the molecular weight of paraquat, C_a^0 (mol/L) is the standard concentration of paraquat (assumed to be 1 mol/L), and γ_a is the activity coefficient (assumed as unity).

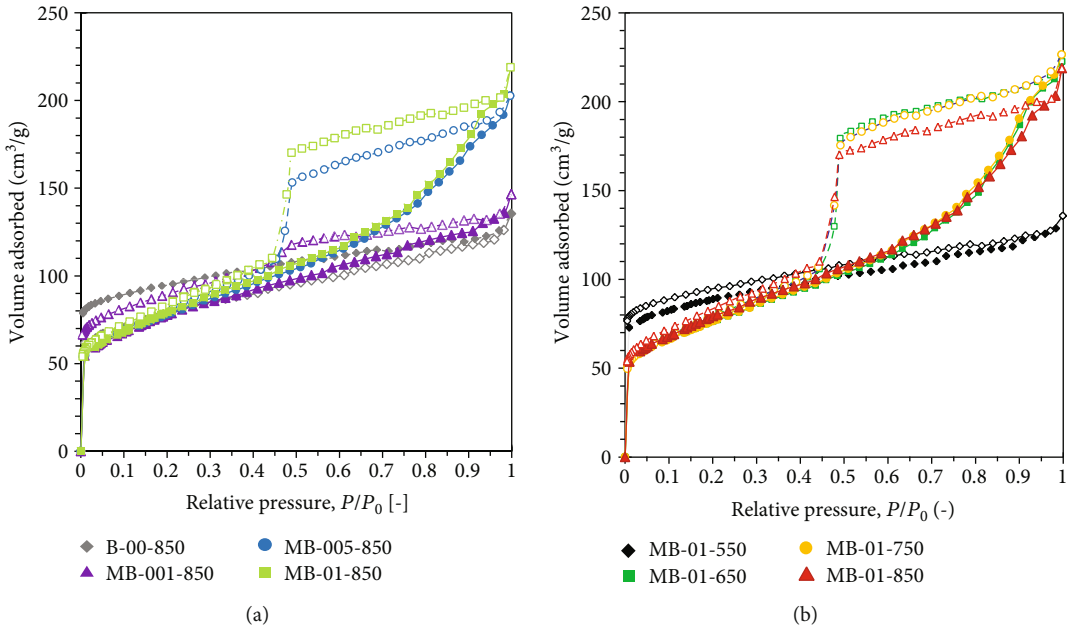

Figure 1: N_2 adsorption-desorption isotherm at -196°C of (a) B-00-850, MB-001-850, MB-005-850, and MB-01-850 and (b) MB-01-550, MB-01-650, MB-01-750, and MB-01-850.

Table 2: N_2 adsorption-desorption isotherm at -196°C and porosity of adsorbents derived from corn husk.

Sample	Type of isotherm	S_{BET} (m^2/g)	V_{mic} (cm^3/g)	V_{meso} (cm^3/g)
B-00-850	I	278.00	0.11	N/D
MB-001-850	I+IV	258.00	0.10	0.10
MB-005-850	I+IV	261.00	0.11	0.28
MB-01-850	I+IV	275.00	0.12	0.30
MB-01-550	I	325.00	0.13	N/D
MB-01-650	I+IV	254.00	0.10	0.35
MB-01-750	I+IV	252.00	0.10	0.35

Remark: N/D = not determined.

ΔH^0 and ΔS^0 were determined from the slope and y -intercept point of the linear plot of ln K^0_{EQ} vs. $1/T$, respectively, and the ΔG^0 was calculated as follows:

$$\Delta G^0 = \Delta H^0 - T\Delta S^0. \quad (7)$$

2.3.3. Kinetic Adsorption Models. Both pseudo-first-order (PFO) and pseudo-second-order (PSO) models were used to determine the kinetic and rate constants.

The original equation of the PFO model proposed by Lagergren [37] is represented by

$$\frac{dq_t}{d_t} = k_1(q_t - q_e). \quad (8)$$

Integrating Equation (9) for $q_0 = 0$ yields [38]

$$q_t = q_e\left(1 - e^{-k_1 t}\right), \quad (9)$$

where k_1 is the rate constant (1/min) and t is the time (min).

The PSO model is widely used for adsorption on solid surface [39]. The original form of the kinetic model is determined by

$$\frac{dq_t}{d_t} = k_2(q_e - q_t)^2, \quad (10)$$

The integrated PSO model is described as follows [38].

$$q_t = \frac{k_2 q_{e2}^2 t}{1 + k_2 q_{e2} t}, \quad (11)$$

$$h_2 = k_2 q_{e2}^2, \quad (12)$$

where k_2 is the constant PSO constant (g/mg·min), q_{e2} is the equilibrium concentration of PQ calculated using the PSO model (mg/g), and h_2 is the initial rate constant (mg/g·min).

The intraparticle diffusion model [40] is calculated by

$$q_t = k_p t^{1/2} + C, \quad (13)$$

where k_p is the rate constant of the intraparticle diffusion model (mg/g·$min^{1/2}$) and C is the thickness of the boundary layer (mg/g).

2.4. Characterization. The specific surface area, micropore volume, and mesopore volume were determined using an

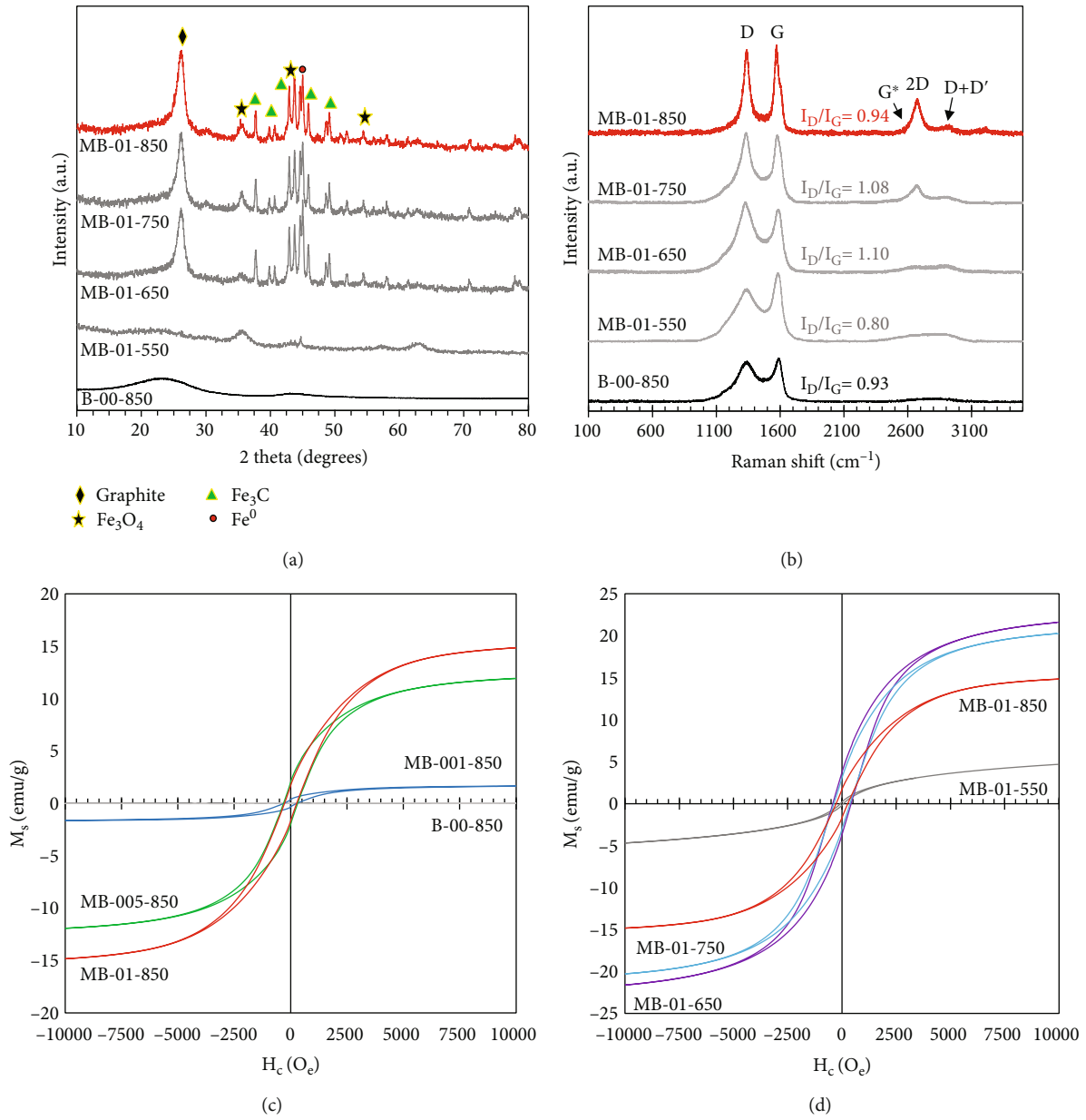

Figure 2: (a) XRD spectra and (b) Raman spectra of B-00-850, MB-01-550, MB-01-650, MB-01-750, and MB-01-850. Magnetization curve of (c) B-00-850, MB-001-850, MB-005-850, and MB-01-850 and (d) MB-01-550, MB-01-650, MB-01-750, and MB-01-850.

Table 3: Magnetic properties of adsorbents.

Sample	Magnetic properties	
	M_s (emu/g)	H_c (O_e)
B-00-850	0.00	0.00
MB-001-850	1.64	290.80
MB-005-850	11.93	313.60
MB-01-850	14.84	270.52
MB-01-750	20.30	371.20
MB-01-650	21.60	421.90
MB-01-550	4.70	67.31

N_2 adsorption-desorption apparatus (Autosorb MP, Quantachrome). The surface morphology was examined using a field emission scanning electron microscope (FE-SEM, JSM-6335F, JEOL) equipped with an energy-dispersive X-ray spectroscopy (EDS) detector (Inca, Oxford). The crystalline phase and iron composition were analyzed using a powder X-ray diffractometer (PXRD; D8 Advanced, Bruker diffractometer with Cu Kα radiation, $\lambda = 1.545$ Å). Raman spectroscopy (Jobin Yvon T64000, HORIBA) was used to study the graphitic features. Magnetic properties were investigated using a vibrating sample magnetometer (VSM, model 73098, Lake Shore). The thermal properties were assessed using a simultaneous thermal analyzer (STA, model 449 F3, Netzsch Jupiter).

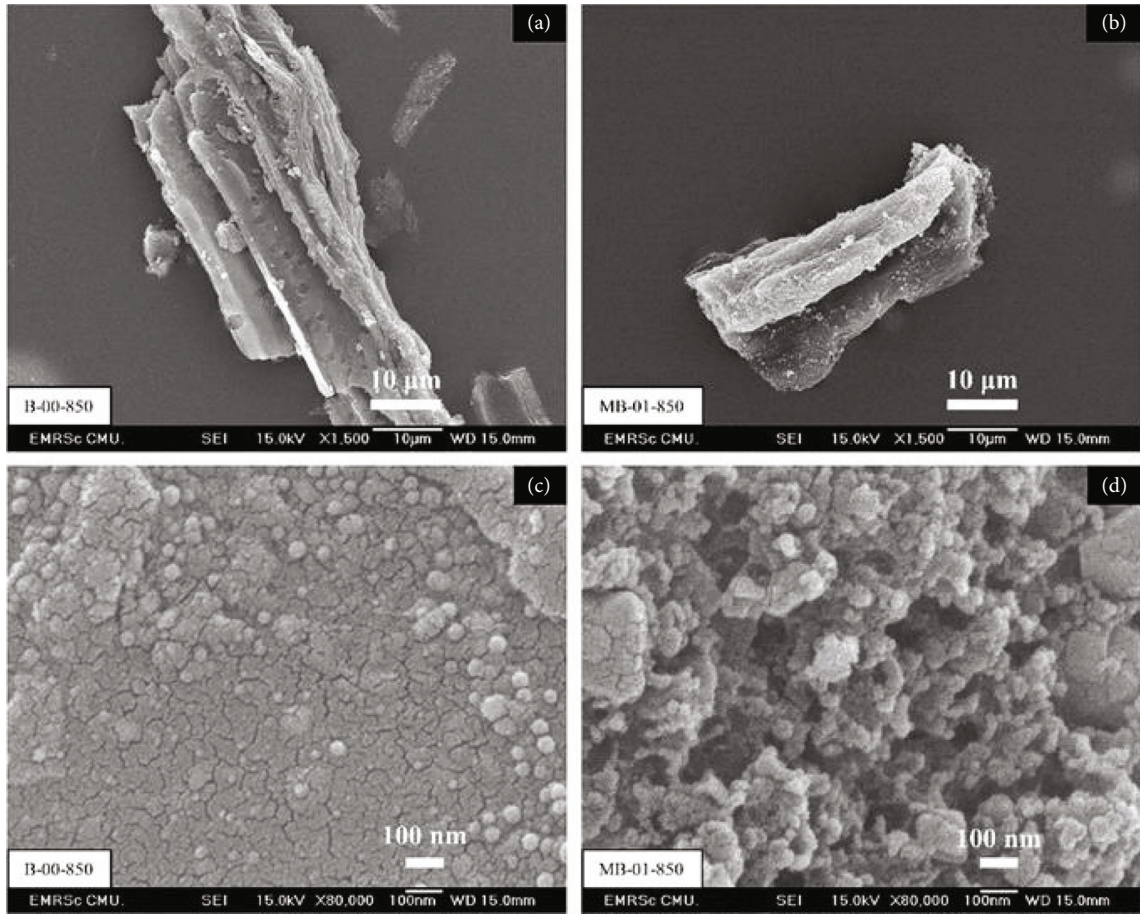

Figure 3: Morphology and surface properties of B-00-850 and MB-01-850.

3. Results and Discussion

3.1. Preparation of Magnetic Biochar

3.1.1. Effect of $Fe(NO_3)_3$ Concentration and Carbonization Temperature on Porosity. Figure 1(a) shows the N_2 adsorption-desorption isotherm of biochar without magnetic properties (B-00-850). It exhibited a type I isotherm according to the IUPAC classification, indicating the presence of a microporous structure (pore diameter < 2 nm) [41]. However, magnetic biochars (MB-001-850, MB-005-850, and MB-01-850) presented a combination of type I and type IV isotherms with an H_3 hysteresis loop, indicating microporous and mesoporous structure [42]. Specific surface area and micro-mesoporous properties were calculated by the BET, DR, and BJH model (Table 2). The results indicated that B-00-850 was only a microporous structure ($V_{micro} = 0.11\,cm^3/g$) and the surface area was $278\,m^2/g$. The micro-mesoporous structures of the samples (MB-001-850, MB-005-850, and MB-01-850) improved with increasing $Fe(NO_3)_3$ concentrations. The micropore volume of the samples was almost $0.10\,cm^3/g$, and the mesoporous volume was $0.10\,cm^3/g$, $0.28\,cm^3/g$, and $0.30\,cm^3/g$ for MB-001-850, MB-005-850, and MB-01-850, respectively. The N_2 adsorption-desorption isotherms of MB-01-550, MB-01-650, MB-01-750, and MB-01-850 are illustrated in Figure 1(b). MB-01-550 displayed a type I isotherm, indicating a microporous structure. On the other hand, MB-01-650, MB-01-750, and MB-01-850 exhibited type I and type IV isotherms with H_3 hysteresis loop characteristics, indicating the existence of microporous and mesoporous structures with plate-like particles. MB-01-550 only shows a microporous structure ($V_{micro} = 0.13\,cm^3/g$, $S_{BET} = 325\,m^2/g$). A mesoporous structure was created when the temperature exceeded 650°C. The mesoporous volume of MB-01-650, MB-01-750, and MB-01-850 was $0.35\,cm^3/g$, $0.35\,cm^3/g$, and $0.30\,cm^3/g$, respectively. The presence of $Fe(NO_3)_3$ at carbonization temperatures lower than 550°C did not generate a mesoporous structure. In conclusion, $Fe(NO_3)_3$ concentration and carbonization temperature play an important role in developing microporous and mesoporous structures [15, 16, 43]. The mesopore size distributions are shown in Figure S3.

3.1.2. Effect of $Fe(NO_3)_3$ Concentration on the Thermal Properties of Corn Husk. Thermogravimetric analysis (TGA) (Figure S2 (a)) revealed that the addition of $Fe(NO_3)_3$ to the corn husk increased its thermal stability compared to that of the untreated corn husk [44]. The residual mass and %burn-off data in Table S1 reinforce this conclusion. The data indicate that the samples with more $Fe(NO_3)_3$ had a lower %burn-off and a higher

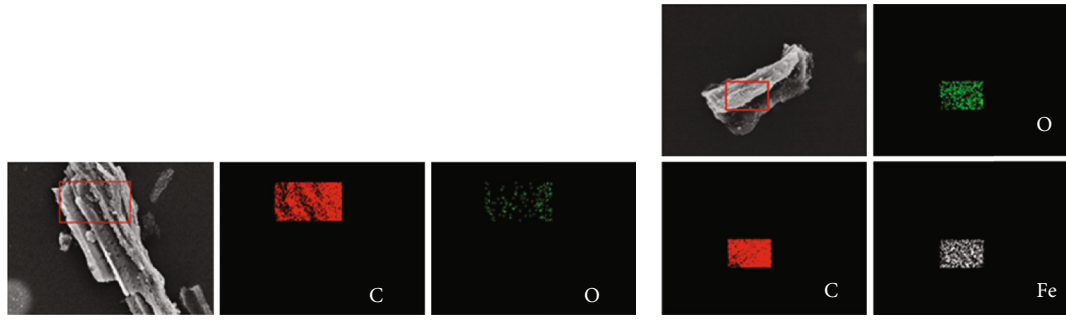

Figure 4: SEM-EDS mapping of (a) B-00-850 and (b) MB-01-850.

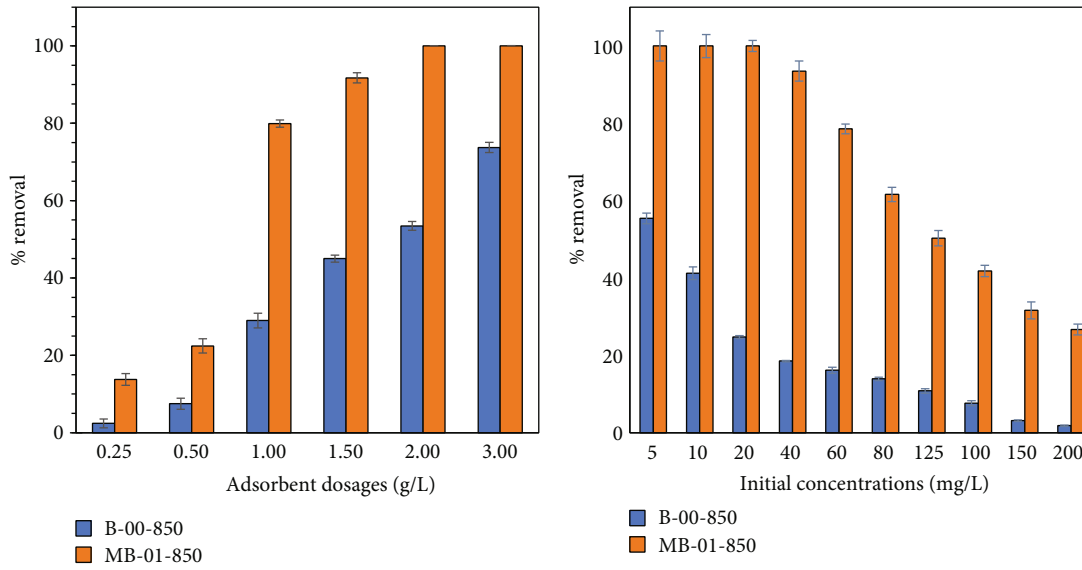

Figure 5: (a) Effect of adsorbent dosages of B-00-850 and MB-01-850 and (b) effect of initial concentrations of B-00-850 and MB-01-850.

residual mass. This suggests that increasing the iron content enhances thermal stability. Figure S2 (b) shows a differential thermogravimetric (DTG) curve, which demonstrates three distinct stages of weight loss. In the first stage, within the temperature range of 32–120°C, an 8.20% weight loss was observed owing to water evaporation. Subsequently, between 180 and 280°C, the thermal decomposition of glycosides, hemicellulose, and pectin units resulted in a weight loss of 32.80%. Finally, at approximately 300°C, a weight loss of approximately 40% indicated cellulose decomposition [45, 46]. A comparative analysis between activated $Fe(NO_3)_3$-treated corn husk and untreated corn husks demonstrated that the former exhibited a distinctive peak in the temperature range of 500–600°C, indicative of the presence of iron compounds. This peak confirmed the formation of iron within the samples, with varying iron concentrations resulting in the formation of iron compounds at slightly different temperatures within the 500–600°C range. Iron compounds can be described as follows: Fe^{3+} ions require hydrolysis to generate amorphous Fe species, including $Fe(OH)_3$ and FeO(OH), below 350°C. Subsequently, the conversion of these amorphous Fe species to Fe_2O_3 was observed at temperatures below 400°C. At higher temperatures (500–700°C), further reduction of hematite (Fe_2O_3) to magnetite (Fe_3O_4) is facilitated by reducing components such as amorphous carbon and CO gas. The formation of metallic Fe was achieved by the reduction of Fe_2O_3 and Fe_3O_4 using amorphous carbon [47–49].

3.1.3. Effect of Carbonization Temperature on Crystallinity. The XRD spectra of B-00-850, MB-01-550, MB-01-650, MB-01-750, and MB-01-850 are shown in Figure 2(a). XRD spectra of MB-01-650, MB-01-750, and MB-01-850 show a sharp peak at 26.20° referring to the graphite phase (JCPDS 01-089-8487). Furthermore, B-00-850 and MB-01-550 exhibited broad peaks at 23.16°, indicating the characteristic peak of amorphous carbon. Clearly, $Fe(NO_3)_3$ carbonized at temperatures above 650°C can improve the formation of graphitic structures and other iron compounds. There were six peaks at 2θ around 37.76°, 42.94°, 43.74°, 44.59°, 48.69°, and 49.14°, including the characteristic peak of iron carbide (Fe_3C) (JCPDS 00-076-1877).

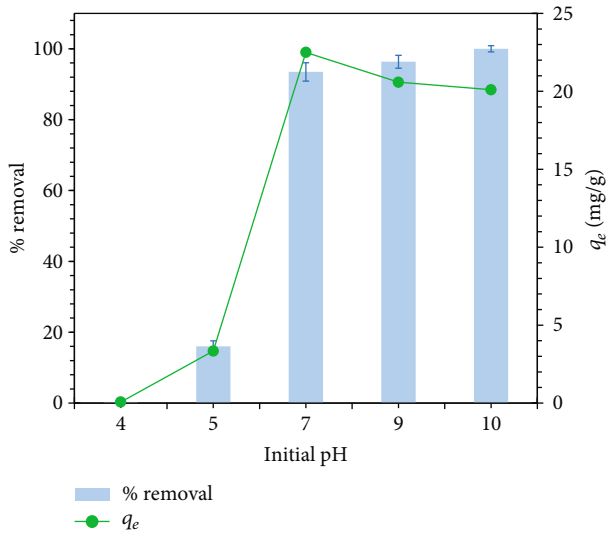

FIGURE 6: Performance of PQ removal in an initial pH range of 4 to 10.

Additionally, the peak appears at 35.35° and 43.74°, showing the characteristic peak (Fe_3O_4) (JCPDS 00-019-0629). Finally, the iron metal is (Fe^0) phase displayed at 45.00° (JCPDS 00-076-1877).

3.1.4. Effect of Carbonization Temperature on Graphitic Characteristic. The Raman spectra of B-00-850, MB-01-550, MB-01-650, MB-01-750, and MB-01-850 are shown in Figure 2(b). All samples show the D band and the G band at 1340 cm^{-1} and 1580 cm^{-1}, respectively, which represent a characteristic feature of graphitic materials. The D band represents local defects and disorders at the edges, which correspond to the out-of-plane vibration of sp^3 defects [50]. The G band is related to the vibration of sp^2 hybridization in the hexagonal graphene structure. Furthermore, the 2D and D+D′ bands at around 2700 cm^{-1} and 2920 cm^{-1} were clearly observed for MB-01-850, indicating that the sample underwent more transformation to the graphitic phase than the other samples [51].

The intensity ratio of the D and G bands (I_D/I_G) serves as a measure of the degree of graphitization and abundance of functional groups present on the surface of the materials. If the ratio is less than 1, the biochar has a high degree of graphitization; if the ratio is greater than 1, a significant number of functional groups are present on the surface of the biochar [52]. As can be seen in Figure 2(b), the I_D/I_G ratio initially increases from 0.80 for MB-01-550 to 1.10 for MB-01-650, after which it decreases to 1.08 for MB-01-750, before finally decreasing to 0.94 for MB-01-850. Increasing the carbonization temperature from 550°C to 750°C increased the I_D/I_G ratio from 0.80 to 1.08, indicating the presence of surface defects resulting from iron oxide formation in the biochars, which is in agreement with the XRD results discussed earlier. However, at 850°C, the I_D/I_G ratio decreased to 0.94, indicating an increasing degree of graphitization when the temperature increased, supporting the presence of a graphitic phase, as indicated by the XRD results.

3.1.5. Magnetic Properties of Adsorbents. Figure 2(c) displays the effect of $Fe(NO_3)_3$ concentration on the magnetization curve. An increase in $Fe(NO_3)_3$ concentration resulted in a higher saturation magnetization (M_s); these were 1.64 emu/g, 11.93 emu/g, and 14.84 emu/g for MB-001-850, MB-005-850, and MB-01-850, respectively (Table 3). The coercive forces (H_c) are 290.80 O_e, 313.60 O_e, and 270.52 O_e for MB-001-850, MB-005-850, and MB-01-850, respectively (Table 3). A hysteresis loop indicates ferromagnetism. The effect of carbonization temperature on the saturation magnetization and coercive force is shown in Figure 2(d). A hysteresis loop appears at temperatures higher than 650°C, indicating ferromagnetism [53]. In contrast, the hysteresis loop did not appear at a carbonization temperature of 550°C because this temperature was insufficient to form Fe_3C, Fe_3O_4, or Fe^0 [54].

3.1.6. Effect of $Fe(NO_3)_3$ on Morphologies and Textures. The morphologies and textures of B-00-850 and MB-01-850 are shown in Figure 3. The morphologies of B-00-850 and MB-01-850 were flakes. The textures exhibited surface roughness and spherical-like particles for B-00-850 and MB-01-850, respectively. Figure 4 shows the distribution of the chemical compositions on the surfaces of B-00-850 and MB-01-850, characterized by SEM-EDS mapping. The distributions of carbon and oxygen were uniform for B-00-850. Carbon, oxygen, and iron were uniformly distributed in MB-01-850. The atomic weight of the sample is listed in Table S2.

3.2. Paraquat Adsorption Test. Microporous adsorbents (B-00-850) and micro-mesoporous adsorbents (MB-01-850) were investigated experimentally.

3.2.1. Effect of Adsorbent Dosage. The effect of adsorbent dosage on the removal of PQ is shown in Figure 5(a). An increase in adsorbent dosage resulted in an increase in the removal percentage (2.42% to 73.33% for B-00-850 and 13.78 to 99.99% for MB-01-850). The removal percentage of MB-01-850 was higher than that of B-00-850 for all adsorbent dosages. The experimental data confirm that mesopores are more efficient at removing PQ than micropores are. The highest removal percentage achieved at an adsorbent dosage of 2.0 g/L was found to be optimal.

3.2.2. Effects of Initial Concentrations and pH. The effect of the initial concentration of PQ in the synthetic water (concentration 5–200 mg/L, pH 7, and 20 h) was studied. Figure 5(b) shows that the PQ removal percentage of MB-01-850 was greater than that of B-00-850, peaking at 99.99% and 55.42% at an initial concentration of 5 mg/L. Moreover, the removal percentage of PQ decreased when the initial concentration of PQ was insufficient due to insufficient adsorption sites.

The effect of pH on PQ adsorption of PQ was examined over a pH range of 4 to 10, as shown in Figure 6. Furthermore, examination of the effects of the initial pH on the

Table 4: Isotherm parameters of the Langmuir and Freundlich models and kinetic parameters of PFO and PSO for PQ adsorption on adsorbents.

Models	Parameters	Synthetic water				Natural water
		B-00-850 (at 30°C)	MB-01-850 (at 30°C)	MB-01-850 (at 40°C)	MB-01-850 (at 50°C)	MB-01-850 (at 30°C)
Langmuir	Q_0 (mg/g)	4.08	34.97	12.69	9.03	31.63
	b (L/g)	0.13	1.82	1.08	0.58	0.90
	R^2 (-)	0.97	0.99	0.99	0.98	0.99
Freundlich	K_F ((mg/g)(L/mg)$^{1/n}$)	0.95	12.76	5.62	4.67	13.40
	n (-)	2.96	3.85	4.63	5.79	4.00
	R^2 (-)	0.99	0.99	0.98	0.99	0.97
PFO	k_1 (1/min)		1.09			
	q_{e1} (mg/g)		8.40			
	R^2 (-)		0.40			
PSO	k_2 (g/mg·min)		0.06			
	q_{e2} (mg/g)		9.59			
	h (mg/g·min)		5.66			
	R^2 (-)		0.99			

adsorption capacity of the sorbent provides insight into the influence of various electrostatic attractions, including ion-dipole or hydrogen bonds. If electrostatic attraction is the predominant factor driving the adsorption mechanism, the adsorption capacity of biochar would be significantly influenced by the pH of PQ adsorption [55, 56]. The PQ adsorption experiments were conducted at an initial concentration, adsorbent dosage, temperature, and contact time of 40 mg/L, 2.0 g/L, 30°C, and 24 h, respectively. An increase in paraquat removal was observed when the pH was increased from 4 to 5, resulting in an increase in PQ removal from 0.33% to 16.02% and an increase in adsorption capacity (q_e) from 0.07 mg/g to 3.34 mg/g. Subsequently, a significant improvement in the removal efficiency was observed with a further increase in the pH from 5 to 7. Within this range, PQ removal increased substantially from 16.02% to 93.48%, and q_e also showed a notable increase, ranging from 3.34 mg/g to 22.50 mg/g.

Additionally, a slight improvement in paraquat removal was observed as pH increased. The investigation yielded PQ removal percentages ranging from 96.34% to 99.99% and q_e ranging from 20.59 mg/g to 20.10 mg/g. These findings demonstrate the influence of pH on the adsorption of PQ, as increasing the pH led to progressively higher removal percentages and enhanced the adsorption capacities.

The observed effect of pH on the adsorption of MB-01-850 can be explained by considering its point of zero charge (pH_{PZC}), as depicted in Figure S4. The pH_{PZC} value for MB-01-850 is 7. When the pH of the solution falls below pH_{PZC}, the surface of the carbon material becomes positively charged, resulting in repulsion of PQ from the carbon surface [57, 58]. Referring to Figure S1, PQ is an organic cation composed of 4,4′-bipyridine with two N-methyl substituents at the 1- and 1′ positions. When the pH of the solution exceeded that of pH_{PZC}, the carbon surface became negatively charged, facilitating attractive interactions between the bipyridinium (N+-benzene ring) in the PQ structure of PQ and the carbon surface [59]. Therefore, based on the results of this experimental investigation, it can be concluded that electrostatic attraction plays a significant role as the primary mechanism governing the adsorption process between the bipyridinium in the PQ structure and MB-01-850.

3.2.3. Equilibrium Isotherms, Thermodynamics, and Kinetic Models. The maximum adsorption capacity (Q_0) was analyzed using the Langmuir model, based on the assumption of monolayer adsorption. At a temperature of 30°C, Q_0 was 4.08 mg/g and 34.97 mg/g for B-00-850 and MB-01-850, respectively. The efficiency of PQ removal can be explained by the theory of adsorption; an appropriate adsorption efficiency occurs when the pore diameter of the adsorbent is larger than 1.7 to 3.0 times of the adsorbate [60]. The dimension of the PQ was 1.34 nm × 0.36 nm [61, 62]. Although MB-01-850 has a pore width of 2.60 nm (Figure S3), approximately 2 times larger than PQ, therefore, this absorbent was more effective for PQ adsorption than B-00-850 because it had only a microporous structure, roughly the same size as PQ. Therefore, the presence of a microporous structure did not increase the PQ adsorption efficiency. The mesopore volume is key for PQ adsorption because of its suitable pore size with the PQ structure. Owing to the low PQ adsorption efficiency of B-00-850, the equilibrium isotherm, kinetics, and thermodynamics of PQ adsorption were only examined for MB-01-850.

The adsorption mechanism of PQ onto MB-01-850 was studied using equilibrium isotherm models. The correlation coefficient (R^2) was used to determine the consistency between experimental and theoretical values (Table 4). Figures 7(b) and 7(c) show that the equilibrium isotherms

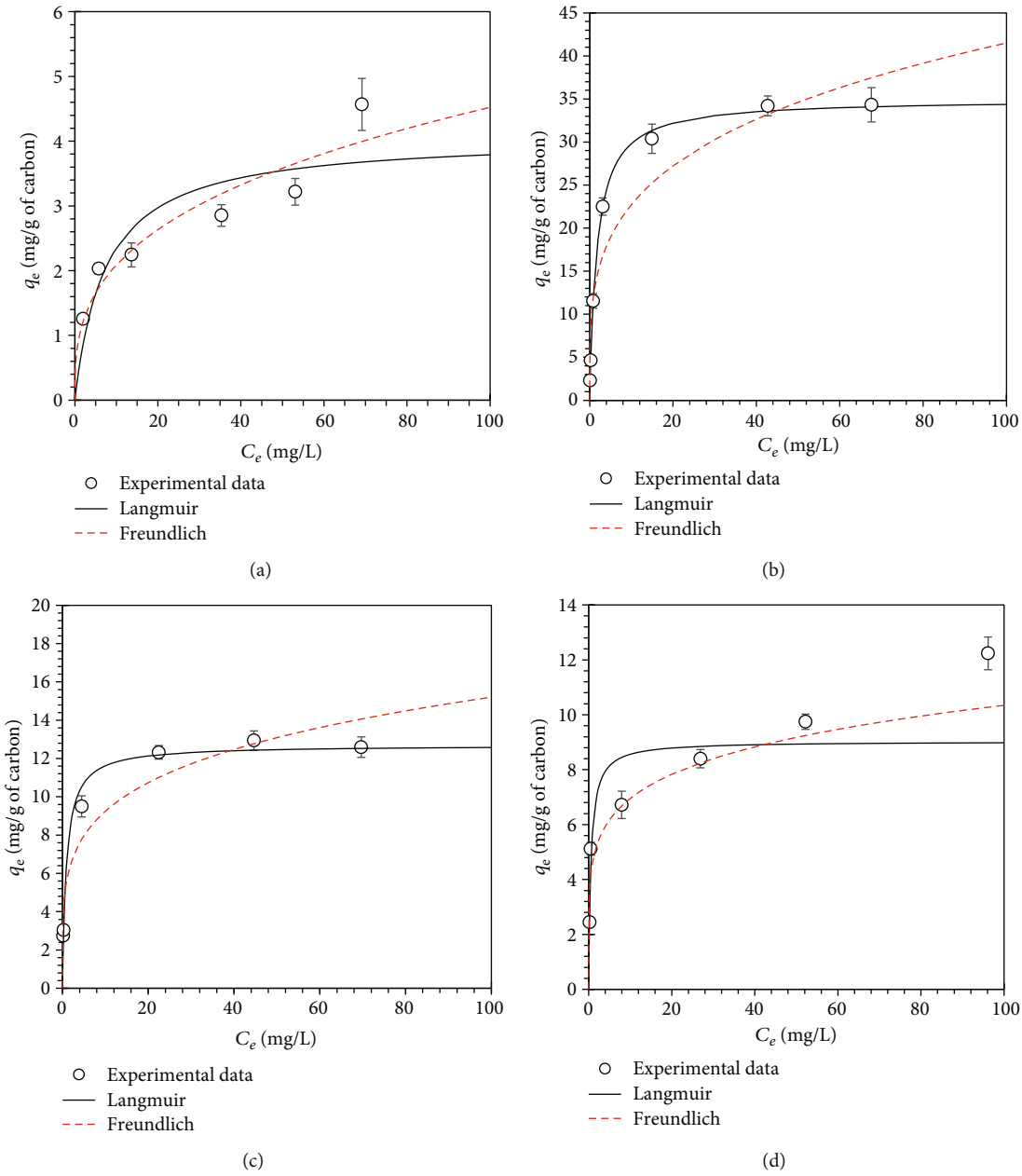

Figure 7: The equilibrium adsorption isotherms of (a) B-00-850 at a temperature of 30°C, (b) MB-01-850 at a temperature of 30°C, (c) MB-01-850 at a temperature of 40°C, and (d) MB-01-850 at a temperature of 50°C.

Table 5: Thermodynamic parameter for PQ adsorption on MB-01-850.

Sample	ΔH^0 (kJ/mol)	ΔS^0 (J/mol·K)	ΔG^0 (kJ/mol)			R^2 (-)
			30°C	40°C	50°C	
MB-01-850	-46.47	-44.62	-32.95	-32.50	-32.05	0.99

of MB-01-850 at 30-40°C fitted better with the Langmuir isotherm model ($R^2 = 0.99$), suggesting that the adsorption was monolayer. MB-01-850 at 50°C (Figure 7(d)) fit better with the Freundlich isotherm model ($R^2 = 0.99$), explaining the multilayer adsorption mechanism [63]. The parameters obtained from the models are listed in Table 4.

In addition, the K^0_{EQ} value derived from the van't Hoff equation was used to calculate the thermodynamic parameters (Table 5). The negative value of ΔH^0 for MB-01-850 (-46.47 kJ/mol) indicated an exothermic adsorption process. The evaluation of the adsorption mechanisms depends on the magnitude of the standard enthalpy change (ΔH^0). Research has shown that if the magnitude of the standard enthalpy change (ΔH^0) is less than 80 kJ/mol, it corresponds to physical adsorption; if it exceeds 200 kJ/mol, it corresponds to chemical adsorption [64]. The adsorption mechanism between PQ and MB-01-850 is physical adsorption,

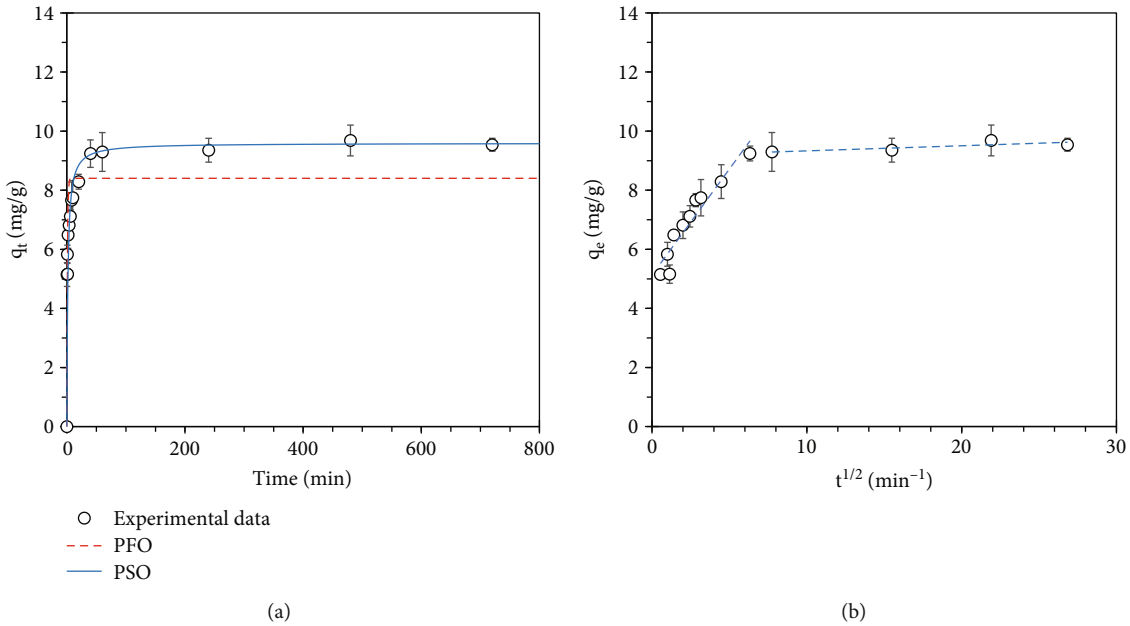

Figure 8: (a) Adsorption kinetics of MB-01-850 at temperature of 30°C and (b) the intraparticle diffusion curve of MB-01-850.

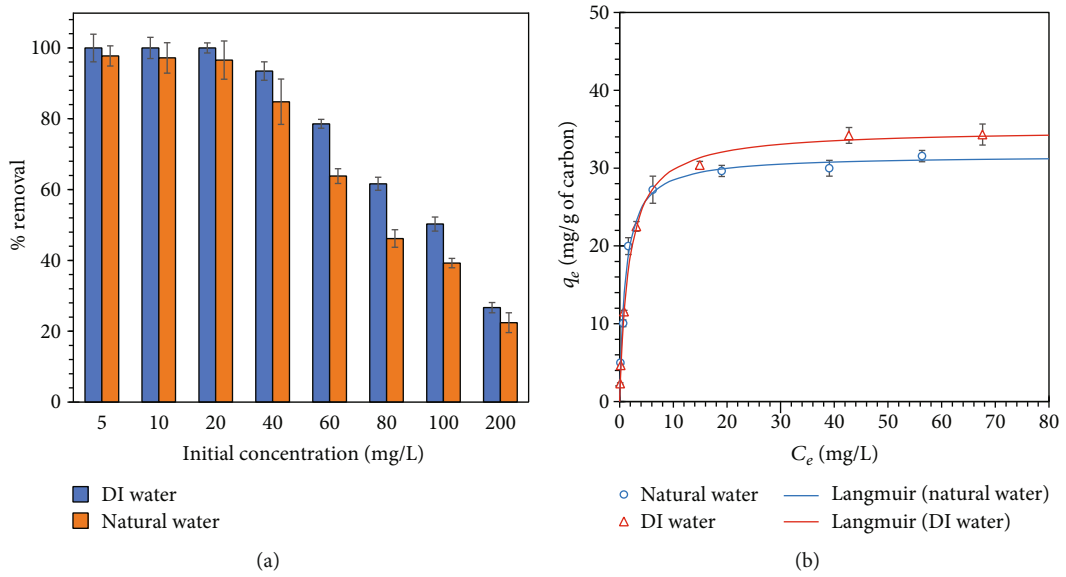

Figure 9: (a) Removal percentage and (b) equilibrium adsorption of PQ in synthetic water and natural water on MB-01-850.

which involves electrostatic attraction, ion-dipole, or hydrogen bonding [64–66]. The adsorption forces may arise from ion-dipole interactions associated with bipyridinium (N +-benzene ring) in the PQ structure, as mentioned in Section 3.2.2, or stem from interactions between the π-electrons in the carbonaceous adsorbent and the π-electrons in the aromatic ring of the adsorbate [56, 67]. The negative ΔS^0 (-44.62 J/mol·K) and ΔG^0 (-32.95, -32.50, and -32.05 kJ/mol for 30, 40, and 50°C, respectively) for MB-01-850 indicate a decrease in randomness at the adsorbent-adsorbate interface and spontaneous adsorption, respectively [68].

Kinetic experiments were performed at an initial concentration of 20 mg/L and 30°C. MB-01-850 reached equilibrium within approximately 20 minutes. These results indicate that the presence of a mesoporous structure enhanced the PQ adsorption rate. The experimental data of MB-01-850 were fitted with R^2 values of PSO models of 0.99, as shown in Figure 8(a). Furthermore, the kinetic parameters for PFO (k_1) and PSO (k_2, h_2) are shown in Table 4, and the initial rate constant (h) is 5.66 mg/g·min that correlated with the reaction rate of the adsorption process. If the regression of q_t versus $t^{1/2}$ is linear and passes through the origin, then intraparticle diffusion is the rate-limiting step [69, 70]. It was found that none of the straight lines passed through the origin; therefore, intraparticle diffusion was not the rate-limiting step. The corresponding

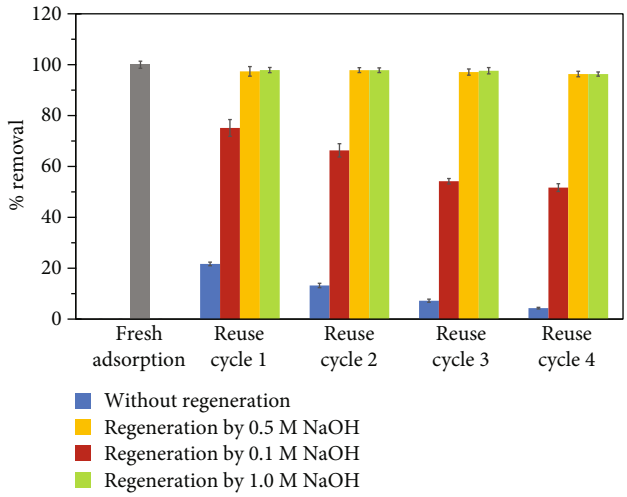

FIGURE 10: Adsorption and regeneration performance of MB-01-850 (initial concentration, 20 mg/L; adsorbent dosage, 2.0 g/L; time, 24 h; temperature, 30°C; and pH, 7).

correlation coefficients and parameters were calculated and are listed in Table S3.

3.2.4. Application to Natural Water. The investigation of the equilibrium adsorption of PQ in various sources, namely, synthetic water and natural water, is illustrated in Figure 9, under PQ concentrations of 5–200 mg/L, temperature of 30°C, and pH of 7. As the concentration of the PQ solution increased, a decrease in the percentage of PQ removed was observed, with values decreasing from 99.99% to 26.68% in synthetic water and from 97.74% to 22.41% in natural water. The adsorption capacities were found to be 34.97 mg/g and 31.63 mg/g for the synthetic water and natural water, respectively, as presented in Table 4. Notably, the adsorption capacity tends to decrease under natural water conditions. This decline can be attributed to the presence of organic substances, metal ions, and other contaminants in natural water, which interfered with the PQ adsorption process on MB-01-850. To support this observation, a reduction in the chemical oxygen demand (COD) value was confirmed after PQ adsorption, decreasing from 17 mg/L to 5.1 mg/L (Table S4).

3.2.5. Reusability of MB-01-850. The reusability of MB-01-850 after several adsorption-desorption cycles is presented in Figure 10. In the absence of the regeneration process, the PQ adsorption efficiency of MB-01-850 significantly decreased. After the first cycle, the PQ of the adsorption and removal percentages decreased to 21.69% and dropped to 4.33% after four cycles. However, the regeneration process involved varying the concentrations of NaOH from 0.1 to 1.0 M. It was observed that a NaOH concentration of 0.1 M resulted in PQ removal percentages ranging from 75.13% to 51.70% after four cycles. Importantly, as the NaOH concentration increased to 0.5 and 1.0 M, a gradual improvement in desorption efficiency was observed. Throughout all four cycles, the PQ removal percentage exceeded 95.00% for NaOH concentrations in the range 0.5 to 1.0 M. The NaOH concentration increased, and the hydroxyl ions interfered with the adsorption between paraquat and the carbon surface charge. As a result, higher NaOH concentrations result in effective regeneration efficiency [71, 72].

For MB-01-850 with and without regeneration, it was evident that the regenerated adsorbent demonstrated excellent adsorption efficiency and could be reused for up to four cycles. These observations highlight the enhanced adsorption performance and increased longevity of the regenerated adsorbent compared to those of the nonregenerated adsorbent.

3.2.6. Comparison of the Current Results with Other Adsorbents. Table 6 comprehensively compares the maximum adsorption capacities of carbon-based and nonporous carbon materials from various related studies [22, 23, 29–31, 59, 73–83]. When evaluating the adsorption efficiency of MB-01-850 compared with carbon-based adsorbents, it was observed to reach a moderate level (Q_0 = 34.97 mg/g). Significantly, this value exceeded the adsorption efficiencies of activated carbon synthesized from spent rubber and nanoporous activated carbon, which recorded values of 16.61 mg/g [74] and 75.80 mg/g [31], respectively. However, Q_0 of MB-01-850 remains lower than that of commercial activated carbon, with a value of 33.70 mg/g [31].

Additionally, compared to noncarbon materials, MB-01-850 exhibited higher adsorption efficiency than several inorganic materials. For example, the bentonite/mesoporous silica compound [77], humic acid-coated goethite [59], kaolin [78], and zeolite Y [82] showed Q_0 values of 11.75 mg/g, 4.40 mg/g, 5.45 mg/g, and 26.38 mg/g, respectively. In summary, the adsorbents used for paraquat removal demonstrated removal efficiencies ranging from 4.40 mg/g to 257 mg/g.

One distinguishing characteristic of MB-01-850 is its ability to be easily separated from the aqueous solution using an external magnet after adsorption, facilitating convenient reuse. Another noteworthy aspect of this research is the practical operating conditions, that is, a pH value of 7, eliminating the need for additional chemicals to adjust the pH. Furthermore, this study used agricultural waste, specifically corn husk, as a precursor material, highlighting its sustainability and ecofriendliness.

4. Conclusions

This study revealed that corn husk carbon can remove paraquat from synthetic and natural wastewater. These results suggest that the presence of $Fe(NO_3)_3$ and carbonization temperatures above 650°C caused the formation of microporous and mesoporous structures, graphitic characteristics, and iron phases. Furthermore, the experimental results demonstrated that the structure of the carbon adsorbent synthesized without $Fe(NO_3)_3$ was microporous. Furthermore, this study provided strong evidence that the mesoporous structure promoted PQ adsorption; the maximum adsorption capacity for MB-01-850 was 34.97 mg/g. In contrast, the microporous structure showed modest adsorption capacities; the highest adsorption capacity for B-00-850 was 4.08 mg/g. Based on the analysis of enthalpy change through

Table 6: Comparison of various adsorbents for removal of PQ.

Adsorbents	Magnetic responsibility	Q_0 (mg/g)	pH	Adsorbent dosage (g/L)	Time (h)	T (°C)	Ref.
Biochar from corn husk	No	4.07	7.0	2.0	20	30	This work
Magnetic biochar from corn husk	Yes	34.97	7.0	2.0	20	30	This work
Activated carbon derived from used tired	No	33.70	7.0	4.0	48	25	[31]
Commercial activated carbon	No	75.80	7.0	4.0	48	25	[31]
Carbon tubes from biomass	No	218.61	NR	0.4	20 min	20	[73]
Nanoporous activated carbon	No	16.61	NR	1.0	5	T_R	[74]
Modified carbon sphere	No	134.63	NR	1.0	30 min	20	[75]
Algerian bentonite	No	100.00	NR	2.0	24	25	[23]
Activated clay	No	58.48	11	2.0	24	25	[29]
Activated bleaching earth	No	34.96	NR	2.0	120 min	25	[30]
Ayous sawdust	No	9.47	NR	6.0	1	25	[76]
Bentonite/mesoporous silica composite	No	11.75	NR	NR	NR	T_R	[77]
Humic acid-coated goethite	No	4.40	4.0	0.6	24	T_R	[59]
Kaolin	No	5.45	NR	2.0	24	23	[78]
Mesoporous silica modified with titania	No	13.68	9.5	6.3	4	25	[79]
Montmorillonite-alginate beads	No	71.49	5.5	NR	6	25	[80]
TEMPO-oxidized cellulose nanofibers	No	108.00	NR	0.1	2	30	[81]
Zeolite LTL	No	166.71	NR	2.5	24	30	[22]
Zeolite Y	No	26.38	6.0	1.0	24	T_R	[82]
Fe_3O_4@SiO_2/SiCRG and Fe_3O_4@SiO_2/SiStarch	Yes	257.00	7.3	0.5	1	25	[83]

Remark: NR = no report; T_R = room temperature.

thermodynamics and investigation of the effect of the initial pH on the adsorption capacity, the findings consistently indicate that electrostatic attraction primarily governs the adsorption process. Furthermore, this adsorbent material exhibits remarkable regenerative capability, which can be regenerated almost completely for at least four cycles using a sodium hydroxide (NaOH) solution with a concentration of 0.5 M or greater.

Data Availability

The data used to support the findings of this study are available from the corresponding authors upon request.

Conflicts of Interest

The authors declare that there is no conflict of interest with respect to the research, authorship, and/or publication of this article.

Authors' Contributions

Sakonsupa Damdib was responsible for methodology, investigation, original draft preparations, and writing—review and editing. Phamornsiri Phamornpiboon and Bhawaranchat Vanichsetakul were assigned for investigation. Chanchana Thanachayanont and Patiparn Punyapalakul were responsible for supervision. Adisak Siyasukh was responsible for conceptualization, methodology, investigation, supervision, original draft preparations, and writing—review and editing. Nattaporn Tonanon was responsible for conceptualization, methodology, supervision, writing—review and editing, and funding acquisition. All authors have read and approved the final manuscript.

Acknowledgments

The authors would like to acknowledge Assistant Professor Dr. Yothin Chimupala from the Department of Industrial Chemistry, Faculty of Science, Chiang Mai University, for consulting the XRD analysis. The authors also sincerely thank the Faculty of Science, Chiang Mai University, and the Bio-Circular-Green Economy Technology and Engineering Center (BCGeTEC), Chulalongkorn University, for supporting and providing the research facilities to carry out this research work. This research project was financially supported by Ratchadapiseksompotch Fund Chulalongkorn University and Thai Graduate Institute of Science and Technology (TGIST), National Science and Technology Development Agency (SCA-CO-2561-6940-TH). This work was also partially supported by Chiang Mai University.

Supplementary Materials

Figure S1: molecular structure of paraquat. Figure S2: (a) TGA curves of B-00-850, MB-001-850, MB-005-850, and MB-01-850 and (b) DTG curves of corn husk and corn husks immersed in $Fe(NO_3)_3$ at concentration of 0.01, 0.05, and 0.10 M. Figure S3: mesopore size distribution of (a) MB-001-850, MB-005-850, and MB-01-850 and (b)

MB-01-650, MB-01-750, and MB-01-850. Figure S4: point of zero charge (pH_{PZC}) of MB-01-850. Table S1: residual mass and %burn-off of corn and corn with activated $Fe(NO_3)_3$. Table S2: chemical compositions of B-00-850 and MB-01-850. Table S3: intraparticle diffusion parameters for PQ adsorption onto MB-01-850. Table S4: chemical oxygen demand (COD) value of natural water with and without PQ. *(Supplementary Materials)*

References

[1] J. Lehmann, J. Gaunt, and M. Rondon, "Bio-char sequestration in terrestrial ecosystems – a review," *Mitigation and Adaptation Strategies for Global Change*, vol. 11, no. 2, pp. 403–427, 2006.

[2] E.-B. Son, K.-M. Poo, J.-S. Chang, and K.-J. Chae, "Heavy metal removal from aqueous solutions using engineered magnetic biochars derived from waste marine macro-algal biomass," *Science of The Total Environment*, vol. 615, pp. 161–168, 2018.

[3] X. Tan, Y. Liu, G. Zeng et al., "Application of biochar for the removal of pollutants from aqueous solutions," *Chemosphere*, vol. 125, pp. 70–85, 2015.

[4] S. Praveen, J. Jegan, T. Bhagavathi Pushpa, R. Gokulan, and L. Bulgariu, "Biochar for removal of dyes in contaminated water: an overview," *Biochar*, vol. 4, no. 1, p. 10, 2022.

[5] J. Wang and S. Wang, "Preparation, modification and environmental application of biochar: a review," *Journal of Cleaner Production*, vol. 227, pp. 1002–1022, 2019.

[6] G. Murtaza, Z. Ahmed, and M. Usman, "Feedstock type, pyrolysis temperature and acid modification effects on physiochemical attributes of biochar and soil quality," *Arabian Journal of Geosciences*, vol. 15, no. 3, p. 305, 2022.

[7] X.-Y. Zeng, Y. Wang, R.-X. Li, H.-L. Cao, Y.-F. Li, and J. Lü, "Impacts of temperatures and phosphoric-acid modification to the physicochemical properties of biochar for excellent sulfadiazine adsorption," *Biochar*, vol. 4, no. 1, p. 14, 2022.

[8] B. Tang, H. Xu, F. Song et al., "Effect of biochar on immobilization remediation of Cd-contaminated soil and environmental quality," *Environmental Research*, vol. 204, no. Part A, article 111840, 2022.

[9] X. Tan, Y. Liu, Y. Gu et al., "Biochar-based nano-composites for the decontamination of wastewater: a review," *Bioresource Technology*, vol. 212, pp. 318–333, 2016.

[10] S. O. Amusat, T. G. Kebede, S. Dube, and M. M. Nindi, "Ball-milling synthesis of biochar and biochar–based nanocomposites and prospects for removal of emerging contaminants: a review," *Journal of Water Process Engineering*, vol. 41, article 101993, 2021.

[11] Y. Yi, Z. Huang, B. Lu et al., "Magnetic biochar for environmental remediation: a review," *Bioresource Technology*, vol. 298, article 122468, 2020.

[12] J. Qu, Z. Li, Z. Wu et al., "Cyclodextrin-functionalized magnetic alginate microspheres for synchronous removal of lead and bisphenol a from contaminated soil," *Chemical Engineering Journal*, vol. 461, article 142079, 2023.

[13] Z. Zhang, G. Huang, P. Zhang, J. Shen, S. Wang, and Y. Li, "Development of iron-based biochar for enhancing nitrate adsorption: effects of specific surface area, electrostatic force, and functional groups," *Science of The Total Environment*, vol. 856, Part 1, article 159037, 2023.

[14] R. Isaac and S. Siddiqui, "Sequestration of Ni(II) and Cu(II) using FeSO4 modified Zea mays husk magnetic biochar: isotherm, kinetics, thermodynamic studies and RSM," *Journal of Hazardous Materials Advances*, vol. 8, article 100162, 2022.

[15] A. Siyasukh, Y. Chimupala, and N. Tonanon, "Preparation of magnetic hierarchical porous carbon spheres with graphitic features for high methyl orange adsorption capacity," *Carbon*, vol. 134, pp. 207–221, 2018.

[16] S. Damdib, N. Vanichsetakul, P. Pimpapoat et al., "Removal of reactive black dye in water by magnetic mesoporous carbon from macadamia nutshell," *Adsorption Science & Technology*, vol. 2022, Article ID 9884474, 17 pages, 2022.

[17] F. W. Oehme and S. Mannala, "Paraquat," in *Small Animal Toxicology*, pp. 964–977, Elsevier, 2006.

[18] C. Berry, C. La Vecchia, and P. Nicotera, "Paraquat and Parkinson's disease," *Cell Death and Differentiation*, vol. 17, no. 7, pp. 1115–1125, 2010.

[19] R. Franco, S. Li, H. Rodriguez-Rocha, M. Burns, and M. I. Panayiotidis, "Molecular mechanisms of pesticide-induced neurotoxicity: relevance to Parkinson's disease," *Chemico-Biological Interactions*, vol. 188, no. 2, pp. 289–300, 2010.

[20] E. Halfon, S. Galassi, R. Brüggemann, and A. Provini, "Selection of priority properties to assess environmental hazard of pesticides," *Chemosphere*, vol. 33, no. 8, pp. 1543–1562, 1996.

[21] G. Veríssimo, J. C. Moreira, and A. Meyer, "Paraquat contamination in surface waters of a rural stream in the mountain region in the state of Rio De Janeiro Southeastern Brazil," *Journal of Environmental and Toxicological Studies*, vol. 2, no. 1, 2018.

[22] W. Insuwan and K. Rangsriwatananon, "Removal of paraquat from aqueous solutions onto zeolite LTL," *Engineering Journal*, vol. 21, no. 2, pp. 15–23, 2017.

[23] D. Ait Sidhoum, M. M. Socías-Viciana, M. D. Ureña-Amate, A. Derdour, E. González-Pradas, and N. Debbagh-Boutarbouch, "Removal of paraquat from water by an Algerian bentonite," *Applied Clay Science*, vol. 83-84, pp. 441–448, 2013.

[24] R. Rajaram and L. Neelakantan, "Recent advances in estimation of paraquat using various analytical techniques: a review," *Results in Chemistry*, vol. 5, article 100703, 2023.

[25] J.-C. Lee, M.-S. Kim, and B.-W. Kim, "Removal of paraquat dissolved in a photoreactor with TiO_2 immobilized on the glass-tubes of UV lamps," *Water Research*, vol. 36, no. 7, pp. 1776–1782, 2002.

[26] M. M. Desipio, R. Thorpe, and D. Saha, "Photocatalytic decomposition of paraquat under visible light by carbon nitride and hydrogen peroxide," *Optik*, vol. 172, pp. 1047–1056, 2018.

[27] M. A. M. Cartaxo, C. M. Borges, M. I. S. Pereira, and M. H. Mendonça, "Electrochemical oxidation of paraquat in neutral medium," *Electrochimica Acta*, vol. 176, pp. 1010–1018, 2015.

[28] A. Dhaouadi and N. Adhoum, "Degradation of paraquat herbicide by electrochemical advanced oxidation methods," *Journal of Electroanalytical Chemistry*, vol. 637, no. 1-2, pp. 33–42, 2009.

[29] W. T. Tsai, C. W. Lai, and K. J. Hsien, "Effect of particle size of activated clay on the adsorption of paraquat from aqueous solution," *Journal of Colloid and Interface Science*, vol. 263, no. 1, pp. 29–34, 2003.

[30] W. T. Tsai, C. W. Lai, and K. J. Hsien, "Adsorption kinetics of herbicide paraquat from aqueous solution onto activated bleaching earth," *Chemosphere*, vol. 55, no. 6, pp. 829–837, 2004.

[31] N. K. Hamadi, S. Swaminathan, and X. D. Chen, "Adsorption of paraquat dichloride from aqueous solution by activated carbon derived from used tires," *Journal of Hazardous Materials*, vol. 112, no. 1-2, pp. 133–141, 2004.

[32] J. Qu, F. Bi, Q. Hu et al., "A novel PEI-grafted N-doping magnetic hydrochar for enhanced scavenging of BPA and Cr(VI) from aqueous phase," *Environmental Pollution*, vol. 321, article 121142, 2023.

[33] I. Langmuir, "The constitution and fundamental properties of solids and liquids. Part I. SOLIDS," *Journal of the American Chemical Society*, vol. 38, no. 11, pp. 2221–2295, 1916.

[34] J. Wang and X. Guo, "Adsorption isotherm models: classification, physical meaning, application and solving method," *Chemosphere*, vol. 258, article 127279, 2020.

[35] H. Freundlich, "Über die adsorption in Lösungen," *Zeitschrift für Physikalische Chemie*, vol. 57U, no. 1, pp. 385–470, 1907.

[36] H. N. Tran, E. C. Lima, R.-S. Juang, J.-C. Bollinger, and H.-P. Chao, "Thermodynamic parameters of liquid–phase adsorption process calculated from different equilibrium constants related to adsorption isotherms: a comparison study," *Journal of Environmental Chemical Engineering*, vol. 9, no. 6, article 106674, 2021.

[37] Y. S. Ho, J. F. Porter, and G. McKay, "Equilibrium isotherm studies for the sorption of divalent metal ions onto peat: copper, nickel and lead single component systems," *Water, Air, and Soil Pollution*, vol. 141, pp. 1–33, 2002.

[38] J. Wang and X. Guo, "Adsorption kinetic models: physical meanings, applications, and solving methods," *Journal of Hazardous Materials*, vol. 390, article 122156, 2020.

[39] Y.-S. Ho, "Review of second-order models for adsorption systems," *Journal of Hazardous Materials*, vol. 136, no. 3, pp. 681–689, 2006.

[40] G. McKay, M. S. Otterburn, and A. G. Sweeney, "The removal of colour from effluent using various adsorbents—III. Silica: rate processes," *Water Research*, vol. 14, no. 1, pp. 15–20, 1980.

[41] K. S. W. Sing, "Reporting physisorption data for gas/solid systems with special reference to the determination of surface area and porosity (recommendations 1984)," *Pure and Applied Chemistry*, vol. 57, no. 4, pp. 603–619, 1985.

[42] M. Thommes, K. Kaneko, A. V. Neimark et al., "Physisorption of gases, with special reference to the evaluation of surface area and pore size distribution (IUPAC technical report)," *Pure and Applied Chemistry*, vol. 87, no. 9-10, pp. 1051–1069, 2015.

[43] D.-W. Cho, K. Yoon, E. E. Kwon, J. K. Biswas, and H. Song, "Fabrication of magnetic biochar as a treatment medium for As(V) via pyrolysis of FeCl3-pretreated spent coffee ground," *Environmental Pollution*, vol. 229, pp. 942–949, 2017.

[44] Y. Dai, Q. Sun, W. Wang et al., "Utilizations of agricultural waste as adsorbent for the removal of contaminants: a review," *Chemosphere*, vol. 211, pp. 235–253, 2018.

[45] J. I. Morán, V. A. Alvarez, V. P. Cyras, and A. Vázquez, "Extraction of cellulose and preparation of nanocellulose from sisal fibers," *Cellulose*, vol. 15, no. 1, pp. 149–159, 2008.

[46] J. Paul Guin, Y. K. Bhardwaj, and L. Varshney, "Radiation grafting: a voyage from bio-waste corn husk to an efficient thermostable adsorbent," *Carbohydrate Polymers*, vol. 183, pp. 151–164, 2018.

[47] S. T. Neeli and H. Ramsurn, "Synthesis and formation mechanism of iron nanoparticles in graphitized carbon matrices using biochar from biomass model compounds as a support," *Carbon*, vol. 134, pp. 480–490, 2018.

[48] X. Zhu, F. Qian, Y. Liu et al., "Controllable synthesis of magnetic carbon composites with high porosity and strong acid resistance from hydrochar for efficient removal of organic pollutants: an overlooked influence," *Carbon*, vol. 99, pp. 338–347, 2016.

[49] P. González-García, "Activated carbon from lignocellulosics precursors: a review of the synthesis methods, characterization techniques and applications," *Renewable and Sustainable Energy Reviews*, vol. 82, pp. 1393–1414, 2018.

[50] Z. Li, X. Li, Y. Zong et al., "Solvothermal synthesis of nitrogen-doped graphene decorated by superparamagnetic Fe_3O_4 nanoparticles and their applications as enhanced synergistic microwave absorbers," *Carbon*, vol. 115, pp. 493–502, 2017.

[51] M. Mohandoss, S. S. Gupta, A. Nelleri, T. Pradeep, and S. M. Maliyekkal, "Solar mediated reduction of graphene oxide," *RSC Advances*, vol. 7, no. 2, pp. 957–963, 2017.

[52] M. B. Ahmed, J. L. Zhou, H. H. Ngo, W. Guo, M. A. H. Johir, and K. Sornalingam, "Single and competitive sorption properties and mechanism of functionalized biochar for removing sulfonamide antibiotics from water," *Chemical Engineering Journal*, vol. 311, pp. 348–358, 2017.

[53] J. Wan, X. Chen, Z. Wang, X. Yang, and Y. Qian, "A soft-template-assisted hydrothermal approach to single-crystal Fe_3O_4 nanorods," *Journal of Crystal Growth*, vol. 276, no. 3-4, pp. 571–576, 2005.

[54] X. Lei, W. Wang, Z. Ye, N. Zhao, and H. Yang, "High saturation magnetization of Fe_3C nanoparticles synthesized by a simple route," *Dyes and Pigments*, vol. 139, pp. 448–452, 2017.

[55] M. C. Ncibi, A. M. B. Hamissa, A. Fathallah et al., "Biosorptive uptake of methylene blue using Mediterranean green alga *Enteromorpha* spp.," *Journal of Hazardous Materials*, vol. 170, no. 2-3, pp. 1050–1055, 2009.

[56] H. N. Tran, Y.-F. Wang, S.-J. You, and H.-P. Chao, "Insights into the mechanism of cationic dye adsorption on activated charcoal: the importance of π–π interactions," *Process Safety and Environmental Protection*, vol. 107, pp. 168–180, 2017.

[57] M. Nasiruddin Khan and A. Sarwar, "Determination of points of zero charge of natural and treated adsorbents," *Surface Review and Letters*, vol. 14, no. 3, pp. 461–469, 2007.

[58] A. K. Dey, A. Dey, and R. Goswami, "Adsorption characteristics of methyl red dye by Na_2CO_3-treated jute fibre using multi-criteria decision making approach," *Applied Water Science*, vol. 12, no. 8, p. 179, 2022.

[59] A. Iglesias, R. López, D. Gondar, J. Antelo, S. Fiol, and F. Arce, "Adsorption of paraquat on goethite and humic acid-coated goethite," *Journal of Hazardous Materials*, vol. 183, no. 1-3, pp. 664–668, 2010.

[60] L. Tang, J. Yu, Y. Pang et al., "Sustainable efficient adsorbent: alkali-acid modified magnetic biochar derived from sewage sludge for aqueous organic contaminant removal," *Chemical Engineering Journal*, vol. 336, pp. 160–169, 2018.

[61] K. Draoui, R. Denoyel, M. Chgoura, and J. Rouquerol, "Adsorption of paraquat on minerals: a thermodynamic study," *Journal of Thermal Analysis and Calorimetry*, vol. 58, pp. 597–606, 1999.

[62] M. Raupach, W. W. Emerson, and P. G. Slade, "The arrangement of paraquat bound by vermiculite and montmorillonite," *Journal of Colloid and Interface Science*, vol. 69, no. 3, pp. 398–408, 1979.

[63] H. K. Boparai, M. Joseph, and D. M. O'Carroll, "Kinetics and thermodynamics of cadmium ion removal by adsorption onto nano zerovalent iron particles," *Journal of Hazardous Materials*, vol. 186, no. 1, pp. 458–465, 2011.

[64] É. C. Lima, M. H. Dehghani, A. Guleria et al., "Adsorption: fundamental aspects and applications of adsorption for effluent treatment," in *Green Technologies for the Defluoridation of Water*, pp. 41–88, Elsevier, 2021.

[65] A. K. Baev, *Specific intermolecular interactions of organic compounds*, Springer Science & Business Media, 2012.

[66] R. Chang and J. W. Thoman Jr., *Intermolecular Forces. Physical Chemistry for the Chemical Sciences*, vol. 792, University Science Books, 2014.

[67] R. W. Coughlin and F. S. Ezra, "Role of surface acidity in the adsorption of organic pollutants on the surface of carbon," *Environmental Science & Technology*, vol. 2, no. 4, pp. 291–297, 1968.

[68] I. A. W. Tan, A. L. Ahmad, and B. H. Hameed, "Adsorption of basic dye on high-surface-area activated carbon prepared from coconut husk: equilibrium, kinetic and thermodynamic studies," *Journal of Hazardous Materials*, vol. 154, no. 1-3, pp. 337–346, 2008.

[69] H. Zheng, D. Liu, Y. Zheng, S. Liang, and Z. Liu, "Sorption isotherm and kinetic modeling of aniline on Cr-bentonite," *Journal of Hazardous Materials*, vol. 167, no. 1-3, pp. 141–147, 2009.

[70] F.-C. Wu, R.-L. Tseng, and R.-S. Juang, "Initial behavior of intraparticle diffusion model used in the description of adsorption kinetics," *Chemical Engineering Journal*, vol. 153, no. 1-3, pp. 1–8, 2009.

[71] A. Larasati, G. D. Fowler, and N. J. D. Graham, "Insights into chemical regeneration of activated carbon for water treatment," *Journal of Environmental Chemical Engineering*, vol. 9, no. 4, article 105555, 2021.

[72] R. J. Martin and W. J. Ng, "Chemical regeneration of exhausted activated carbon—II," *Water Research*, vol. 19, no. 12, pp. 1527–1535, 1985.

[73] H. Li, H. Qi, M. Yin, Y. Chen, Q. Deng, and S. Wang, "Carbon tubes from biomass with prominent adsorption performance for paraquat," *Chemosphere*, vol. 262, article 127797, 2021.

[74] N. Mueanpun, N. Srisuk, N. Chaiammart, and G. Panomsuwan, "Nanoporous activated carbons derived from water ferns as an adsorbent for removal of paraquat from contaminated water," *Materialia*, vol. 15, article 100986, 2021.

[75] H. Li, Q. Miao, Y. Chen et al., "Modified carbon spheres as universal materials for adsorption of cationic harmful substances (paraquat and dyes) in water," *Microporous and Mesoporous Materials*, vol. 297, article 110040, 2020.

[76] C. P. Nanseu-Njiki, G. K. Dedzo, and E. Ngameni, "Study of the removal of paraquat from aqueous solution by biosorption onto Ayous (*Triplochiton schleroxylon*) sawdust," *Journal of Hazardous Materials*, vol. 179, no. 1-3, pp. 63–71, 2010.

[77] Z. Dehgani, M. Sedghi asl, M. Ghaedi, M. M. Sabzehmeidani, and E. Adhami, "Removal of paraquat from aqueous solutions by a bentonite modified zero-valent iron adsorbent," *New Journal of Chemistry*, vol. 44, pp. 13368–13376, 2020.

[78] D. A. Martins, M. Simões, and L. Melo, "Adsorption of paraquat dichloride to kaolin particles and to mixtures of kaolin and hematite particles in aqueous suspensions," *Journal of Water Security*, vol. 1, no. 1, pp. 25–36, 2015.

[79] M. Brigante and P. C. Schulz, "Adsorption of paraquat on mesoporous silica modified with titania: effects of pH, ionic strength and temperature," *Journal of Colloid and Interface Science*, vol. 363, no. 1, pp. 355–361, 2011.

[80] M. Etcheverry, V. Cappa, J. Trelles, and G. Zanini, "Montmorillonite-alginate beads: natural mineral and biopolymers based sorbent of paraquat herbicides," *Journal of Environmental Chemical Engineering*, vol. 5, no. 6, pp. 5868–5875, 2017.

[81] C.-F. Huang, C.-W. Tu, R.-H. Lee, C.-H. Yang, W.-C. Hung, and K.-Y. Andrew Lin, "Study of various diameter and functionality of TEMPO-oxidized cellulose nanofibers on paraquat adsorptions," *Polymer Degradation and Stability*, vol. 161, pp. 206–212, 2019.

[82] R. Sirival, N. Patdhanagul, S. Preecharram, and S. Photharin, "Removal of paraquat solution onto zeolite material," *AIP Conference Proceedings*, vol. 1954, article 030006, 2018.

[83] T. Fernandes, S. F. Soares, T. Trindade, and A. L. Daniel-da-Silva, "Magnetic hybrid nanosorbents for the uptake of paraquat from water," *Nanomaterials*, vol. 7, no. 3, 2017.